Volume 12 | Issue 2 Article 1

Synthesis and Characterization of Ti-Enhanced F75/HA Functionally Graded Materials Fabricated by Powder Metallurgy

Afrah M. Al Hussainey
Physics Dept., College of Science, Mustansiriyah University, Baghdad, Iraq., Afrah77@uomustansiriyah.edu.iq

Aseel Mustafa
Physics Dept., College of Science, Mustansiriyah University, Baghdad, Iraq.

Randa Kamel Hussain
Physics Dept., College of Science, Mustansiriyah University, Baghdad, Iraq.

Synthesis and Characterization of Ti-Enhanced F75/HA Functionally Graded Materials Fabricated by Powder Metallurgy

Abstract

Functionally graded materials (FGMs) are a highly advanced class of biomaterials with graded structure and properties, enabling the fabrication of physiologically and mechanically compatible materials for use in various medical devices. This study aims to produce a functional-grade material based on a cobalt-chromium-molybdenum alloy (F75) reinforced with 4% titanium (Ti) and hydroxyapatite (HA). This will enhance the material's mechanical properties, corrosion resistance, and bioactivity, making it suitable for use as a bone substitute. The natural eggshells were washed, burnt, and chemically processed to form hydroxyapatite with a Ca/P proportion of 1.67. FTIR showed that phosphate and OH groups were separate, and XRD showed that the substance formed nano-HA (peaks at 25.9 ° and 49.5 ° with a crystallite size of 14-56 nm), which showed the purity of the substance.

Five-layer graded materials (FGM) were created using the prepared HA. With an elastic modulus of 34.37±0.49 GPa, which is closer to that of natural bone and lessens stress shielding, FGM performed the best. Additionally, its corrosion rate dropped to 0.413±0.015 mm/y, and its hardness rose to 375.63±17.8 HV. In terms of biology, FGM exhibited a high bio-sedimentation rate (90%) during immersion, and the number of bacterial colonies decreased from $1.34 \pm 0.02 \times 10^8$ CFU/ml to $0.060 \pm 0.020 \times 10^8$ CFU/ml, yielding an inhibition rate of more than 95%. Titanium's ability to reduce crystalline defects and form a stable Tio_2 layer that enhances corrosion resistance and bioactivity is responsible for these advancements. This study demonstrates the effectiveness of titanium in developing functionally graded materials for use as bone implants.

Keywords

Hydroxyapatite, F75 alloy, Titanium, Functionally Graded Materials, Microscopic Hardness, Antibacterial.

This research paper is available in Karbala International Journal of Modern Science: https://kijoms.uokerbala.edu.iq/home/vol12/iss2/1

RESEARCH PAPER

Synthesis and Characterization of Ti-enhanced F75/HA Functionally Graded Materials Fabricated by Powder Metallurgy

Afrah M. Al Hussainey*, Aseel M. Abdul Majeed, Randa K. Hussain

Physics Dept., College of Science, Mustansiriyah University, Baghdad, Iraq

Abstract

Functionally graded materials (FGM) are a highly advanced class of biomaterials with graded structure and properties, enabling the fabrication of physiologically and mechanically compatible materials for use in various medical devices. This study aims to produce a functional-grade material based on a cobalt-chromium-molybdenum alloy (F75) reinforced with 4 % titanium (Ti) and hydroxyapatite (HA). This will enhance the material's mechanical properties, corrosion resistance, and bioactivity, making it suitable for use as a bone substitute. The natural eggshells were washed, burnt, and chemically processed to form hydroxyapatite with a Ca/P proportion of 1.67. FTIR showed that phosphate and OH groups were separate, and XRD showed that the substance formed nano-HA (peaks at 25.9° and 49.5° with a crystallite size of 14−56 nm), which showed the purity of the substance.

Five-layer graded materials (FGM) were created using the prepared HA. With an elastic modulus of 34.37 ± 0.49 GPa, which is closer to that of natural bone and lessens stress shielding, FGM performed the best. Additionally, its corrosion rate dropped to 0.413 ± 0.015 mm/y, and its hardness rose to 375.63 ± 17.8 HV. In terms of biology, FGM exhibited a high bio-sedimentation rate (90 %) during immersion, and the number of bacterial colonies decreased from 1.34 ± 0.02 × 10^8 CFU/ml to 0.060 ± 0.020 × 10^8 CFU/ml, yielding an inhibition rate of more than 95 %. Titanium's ability to reduce crystalline defects and form a stable Tio_2 layer that enhances corrosion resistance and bioactivity is responsible for these advancements. This study demonstrates the effectiveness of titanium in developing functionally graded materials for use as bone implants.

Keywords: Hydroxyapatite, F75 alloy, Titanium, Functionally graded materials, Microscopic hardness, Antibacterial

1. Introduction

Metallic materials are widely used in the fabrication of load-bearing bone implants due to their mechanical strength, durability, and excellent corrosion resistance [1]. Among these materials, cobalt-chromium-molybdenum alloys, particularly the standard ASTM F75 alloy, are widely used in artificial joints and bone implants due to their high wear resistance and long-term structural stability [2]. However, these alloys suffer from a fundamental problem: they have a Young's modulus much higher than that of natural bone. This leads to mechanical incompatibility and stress shielding, which cause the surrounding bone to gradually resorb and, over time, lead to implant failure or loosening [3].

To improve the biocompatibility of these alloys, bioactive ceramic phases were incorporated with the mineral materials. The most significant of these materials is hydroxyapatite (HA), which closely resembles the mineral component of natural bone and can facilitate cell adhesion and establish a true connection between the bone and the implant [4]. However, its high fragility and low mechanical strength limit its use as a single-implant material, particularly in load-bearing applications [5].

Received 22 December 2025; revised 9 February 2026; accepted 14 February 2026.
Available online 12 March 2026

* Corresponding author.
E-mail address: Afrah77@uomustansiriyah.edu.iq (A.M. Al Hussainey).

https://doi.org/10.33640/2405-609X.3453

Titanium and its stable surface oxide layer (Tio_2) have also garnered significant attention in the biomedical field due to their excellent biocompatibility, high corrosion resistance, and ability to enhance osseointegration. The Tio_2 layer reduces the release of metal ions, reduces inflammatory responses, and improves the long-term biocompatibility of metal implants [6]. However, adding titanium alone does not fully resolve the problem of mechanical incompatibility between the implant and bone.

In this context, functionally graded materials (FGM) have emerged as a promising engineering solution to address the mechanical and biological gap between metal implants and natural bone. These materials exhibit gradual changes in composition, microstructure, and properties across their thickness, enabling integration of a highly durable metal core with biocompatible ceramic surface layers. This gradual change minimizes abrupt variations in Young's modulus at the implant-bone interface, reduces stress concentration, and improves long-term implant stability [7].

The study by Z. Doni and colleagues showed that adding hydroxyapatite to alloy F75 increased the rate of localized corrosion at pore sites [8]. M. Fellah and his colleagues also showed that the more the F75 alloy powders are ground, the greater their corrosion resistance [9]. A study by X. Hu and others showed that titanium surfaces possess antibacterial activity associated with the generation of reactive oxygen species; in contrast, cobalt and chromium alloys, whose surfaces are treated, reduce bacterial adhesion primarily by altering the surface chemical composition and increasing hydrophilicity [28].

Bahrami et al. proved that strengthening cobalt, chromium, molybdenum, or titanium alloys with hydroxyapatite leads to a decrease in the modulus of elasticity due to agglomeration and porosity [24].

However, these and other studies focused on traditional coatings or composite materials and did not support the F75 alloy with titanium [20,27], the current research aims to manufacture a functionally graded material based on the ASTM F75 alloy reinforced with hydroxyapatite and titanium and to study the effect of this addition on the material's mechanical and biological properties, thereby contributing to the development of advanced bone implants with improved biocompatibility.

2. Materials and methods

2.1. Preparation of HA

Phosphoric acid and eggshells were used to make hydroxyapatite powder. After cleaning and drying, the shells were calcined at 1000 °C to produce calcium oxide. Calcium phosphate was produced by crushing the calcined shells and mixing them with phosphoric acid at a 1:1 weight ratio. A planetary ball mill was used to achieve homogeneity and prevent clumping of the mixture, which was recalcined at 1000 °C for 2 h. Particle size distributions were obtained using a BETiser 2000 laser particle analyzer. The particle size distribution of HA (0.8–27 μm) spans the nanoscale and microscale, enhancing biocompatibility when used as an active layer.

2.2. Preparation of F75/HA FGM

This study used raw cobalt, chromium, and molybdenum powders, purchased from Sigma-Aldrich Chemicals P. Ltd., to prepare a Co–Cr–Mo (F75) alloy. The particle sizes were 16.4 μm, 26.2 μm, and 13.6 μm, respectively. The powders were thoroughly mixed to achieve the desired alloy composition. Pre-prepared (HA) powder from eggshells and F75 alloy powder (63Co–27Cr–6Mo) modified with 4 % wt % titanium (F75–Ti) were combined to fabricate five-layer functional graded materials (FGM). The HA/F75–Ti ratios were carefully designed to achieve a gradual structural transition and minimize mechanical differences between the layers. Table 1 illustrates the preparation methodology and the resulting graded structural model.

The powders were weighed with an accuracy of ±0.0001 using a sensitive balance type (L220S–D), then mixed using an electric mixer (STGQM–1/5-2) to obtain a homogeneous distribution. Stainless steel balls of different diameters were used, and a specific amount of alcohol was added to reduce friction and prevent oxidation during the 6–h mixing process. After that, the powders were filled into the mold in a controlled, successive-stage manner. An electromechanical-hydraulic press was used to compress the samples to 500 MPa. The green density of the samples before sintering was calculated using the volumetric density law, yielding a value of 3.7 g/cm^3.

Table 1. Model of FGM profile.

Thickness (mm)	Chemical Analysis (%)	Layers
0.5	50HA-50F75	1st
0.75	55F75-45HA	2nd
1	65F75-35HA	3rd
1.25	75F75-25HA	4th
1.5	85F75-15HA	5th

The resulting samples were then heated in a vacuum furnace (GSL–1500X–50 Compact) under an inert gas (argon) atmosphere, according to the heating program shown in Fig. 1.

There were three primary phases to the sintering program. To prevent thermal expansion discrepancies between the layers, the first stage began with dehumidification at 25 °C. It was then heated to 200 °C at 2 °C/min without cracking. The second stage involved stabilizing the primary structure at 200–400 °C, 120 min, followed by heating to 400–1000 °C at 5 °C/min to remove primary porosity without cracking. The actual sintering process, which resulted in the formation of the grain necks, and bonding took place between them, with a sufficient residence time to guarantee the homogeneity of the grains and the bonding of the FGM layers, depending on the slow drop in temperature to room temperature at a rate of 5 °C/min to minimize cracking, alter the HA microstructure, and eliminate any remaining stresses. The density of the sintered portion was calculated in accordance with ASTM B328-96 and was 4.6 g/cm^3.

2.3. Material characterizations

2.3.1. Structural and mechanical characterization

Functional groups were identified in the prepared materials by chemically, structurally, and microscopically characterizing them using Fourier transform infrared spectroscopy (FTIR) with a Shimadzu IRAffinity-1 spectrophotometer at a wavenumber of 4000–400 cm^{-1} with a resolution of 4 cm^{-1}. The crystal structure and phases formed were then investigated by X-ray diffraction (XRD). A Shimadzu LabX device with Cu Kα copper radiation (λ = 1.542 Å), an operating voltage of 40 kV, a current of 30 mA, and a scanning range of 10°–80° (2θ) was used for the XRD analysis.

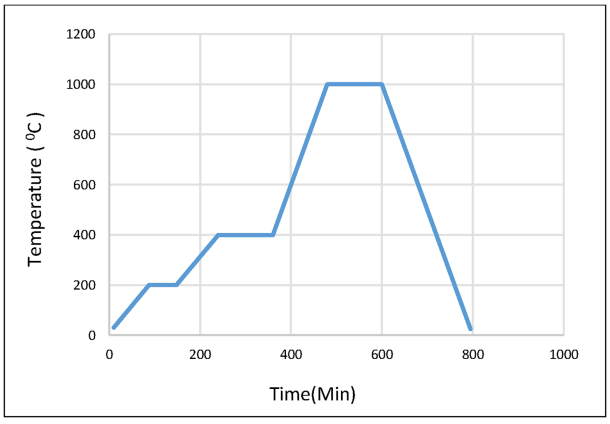

Fig. 1. Sintering cycle representation.

Scanning electron microscopy (SEM; FEI Inspect F50) was also used to examine the surface structure and element distribution at an acceleration voltage of 25 kV.

The crystal size (D) was determined using Shearer's formula [9]:

$$\beta = \frac{k\lambda}{D\cos\theta} \tag{1}$$

The Williamson–Hall equation was used to determine the micro strain [9]:

$$\beta \cos\theta = 4\epsilon \sin\theta + \frac{k\lambda}{D} \tag{2}$$

Mechanical properties, including microhardness and modulus of elasticity, were also evaluated.

The polished surfaces of the samples were measured for microhardness using a Vickers hardness tester (type Hv-1000) with a diamond Vickers pyramid, with a load of 0.98 N applied for 15 s. The mean of at least 10 readings was used as the final result.

The elastic modulus of the samples was determined using ultrasonic pulse-echo technology with a CSi CCT-4 device. The longitudinal and shear wave velocities (V_p and V_s) were measured using 5 MHz probes with the application of coupling gel. The dimensions and thickness of the sample were recorded to accurately calculate the transit time. The density (ρ) was also calculated from the mass-to-volume ratio. The modulus of elasticity was calculated using the equation [10]:

$$E = \frac{\rho V_s^2\left(3V_p^2 - 4V_s^2\right)}{\left(V_p^2 - V_s^2\right)} \tag{3}$$

All measurements were conducted at room temperature, and the final reading was the average of five readings per sample.

2.3.2. Corrosion tests

The dynamic potential polarization test was performed in simulated body fluid (SBF) solution prepared according to the Kokubo protocol [11], after mechanically polishing the samples to 1200 grit and ultrasonically cleaning them in ethanol. Measurements were performed using a Potentiostat/Galvanostat, and the Ecorr and Icorr values were extracted from the polarisation curves via Tafel analysis. Tests were conducted on five independent samples (n = 5), and the corrosion rate was calculated from the corrosion current density using Faraday's law, which relates the alloy's equivalent weight to its density. The corrosion rate is expressed in mm/year.

2.3.3. Biological and bioactivity tests

To assess the bioactive behavior of the samples, an immersion test in a body fluid-mimicking solution (SBF) was conducted. This is performed regularly to demonstrate similarity in the in vitro and in vivo behavior. The samples were prepared using standard mineralogical methods, and all sintered samples were incubated in SBF solution in a clean bottle for 48 days. The samples were tested for antibacterial activity against Gram-negative *Escherichia coli* and Gram-positive *Staphylococcus aureus*. Bacteria were cultivated in Mueller–Hinton broth at 37 °C for 24 h. The bacterial suspension was set up in sterile distilled water, and its turbidity was adjusted to the McFarland standard (1.5×10^8 CFU/mL). The suspension was diluted, mixed with Mueller–Hinton medium, and added to tubes containing the samples; a tube without a sample served as the positive control [12].

3. Results and discussion

3.1. Structural characterization

3.1.1. FTIR spectrum

The FTIR spectrum of hydroxyapatite, which displays distinctive peaks confirming its production, is displayed in Fig. 2. The integrity of the hydroxylated structure is indicated by the sharp peaks at 3570 and 3510 cm^{-1} in Table 2, which are caused by stretching vibrations of the (OH^-) structural group in the HA crystal structure. The (CO_3^{2-}) group's vibrations are responsible for the peak at 1427 cm^{-1}, indicating carbonate substitution within the carbonated HA crystal structure. This is a common characteristic of biogenic hydroxyapatite found in natural bones. Phosphate groups (PO_4^{3-}) exhibit characteristic peaks at 1103 and 1049 cm^{-1} (asymmetric stretching vibration), 964 cm^{-1} (symmetric vibration), and 609 and 563 cm^{-1} (bending vibrations), in addition to the peak at 439 cm^{-1} (bending) [13].

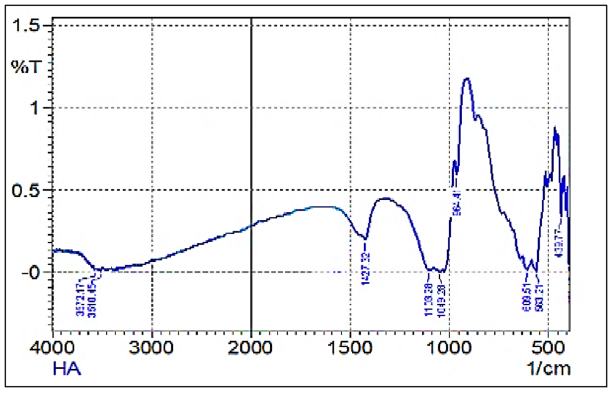

Fig. 2. HA from eggshells FT-IR spectrum.

Table 2. The significant FT-IR stretching of HA frequencies from the eggshell.

Bands of Infrared Absorption	Description
439	PO_4^{-3} Bending
563	PO_4^{-3} Bending
609	PO_4^{-3} Bending
964	Symmetric stretching PO_4^{-3}
1049	Asymmetric stretching PO_4^{-3}
1103	Asymmetric stretching PO_4^{-3}
1427	CO_3
3510	OH Bending
3572	OH Bending

3.1.2. X-ray diffraction

Fig. 3 displays the hydroxyapatite powder produced from eggshells' X-ray diffraction pattern in comparison to the pure hydroxyapatite reference standard pattern (JCPDS No. 09-0432). At the angles ($2\theta \approx 25.4°$, 31.7°, 32.9°, 34.0°, and 37.3°), which correspond to the crystalline planes (002), (211), (300), (202), and (310), respectively, the results revealed the appearance of distinct diffraction peaks. This is the same as the hexagonal crystalline phases of pure hydroxyapatite $Ca_{10}(PO_4)_6(OH)_2$ [14]. The produced material has a consistent crystalline structure and is free of secondary phases, such as tricalcium phosphate (TCP), as evidenced by its peak positions and intensities matching those of the reference pattern. This attests to the effectiveness of the preparatory procedure and the

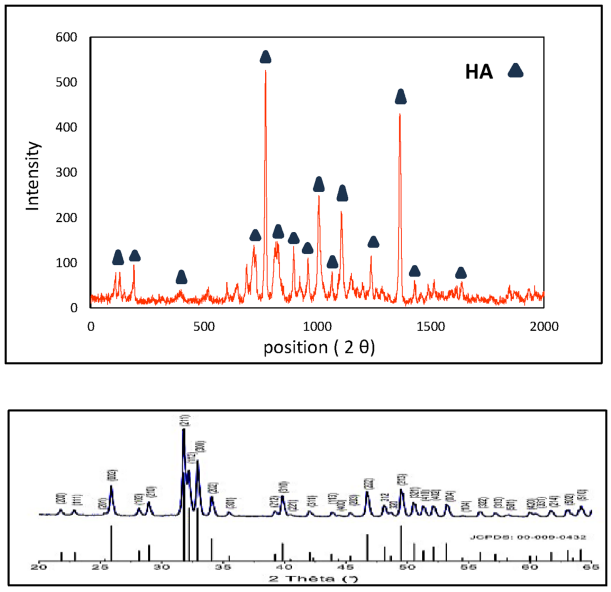

Fig. 3. XRD spectrum for the resulting HA of eggshells and of pure hydroxyapatite.

material's purity, sharpness of the edges, and the clarity of the peaks are also indicators of high crystallinity, which enhances the material's stability and chemical stability in biological applications, particularly as a biocompatible surface in functional graded materials (FGM) with F75 alloy.

Crystalline size of the prominent peaks was determined by applying the Scherrer equation (1) to the X-ray diffraction data with a Cu source ($\lambda = 1.542$ Å), where the half-intensity width (FWHM) of each peak was determined, and Williamson–Hall analysis (as equation (2)) was used to determine strain (ϵ), as is presented in Table 3. The values in the table show that the crystal size ranges from 14 to 56 nm, with an average of approximately 36 nm, clearly indicating that the prepared hydroxyapatite is nanocrystalline [15]. This structural pattern is a key advantage in biological applications, as it provides a high surface area that enhances ion-exchange activity (Ca^{2+} and PO_4^{3-}) and accelerates the formation of a secondary apatite layer upon immersion in simulated body fluid (SBF). Nano-crystalline surface technology also provides nano-topography similar to that of natural bone, increasing osteoblast adhesion and stimulating bone growth [16].

The matching of the (2θ) and (d) values with the standard HA card confirms that the crystalline phase is pure. The various values of FWHM are used to accurately estimate D, where a larger peak width means smaller, more bioactive crystals. Sharp peaks such as (002) and (211) indicate large, stable crystals, while broad peaks such as (102) reflect small nanocrystals with a high surface area that promote (Ca^{2+}/PO_4^{3-}) ion exchange.

Higher strain (ε) values at low-angle peaks (e.g., 26.49° and 28.73°) indicate lattice stresses resulting from crystal defects or a lack of internal symmetry, consistent with the observed small crystal size. Peaks at high angles reflect lower strain, indicating improved lattice regularity with increasing crystallinity [17].

The Dislocation distance indicates the degree of crystal regularity. The smaller the value, the greater the dislocations, indicating that the material is under greater internal stress. At low-angle peaks (26–28°), the crystals are tiny (D ≈ 14–20 nm), and the dislocations are close together (≈8 nm), indicating high internal stresses. At the intermediate peaks (30–35°), the crystals begin to form regularity (D ≈ 27–32 nm), and the spacing between dislocations increases (D ≈ 12–15 nm). At the high peaks (37–47°), the dislocation distance increases to 17–26 nm, indicating an improved crystalline arrangement and reduced stresses, suggesting that the crystallization process has successfully formed regular nano-HA [18].

The X-ray diffraction patterns of the functionally graded samples (Fig. 4) revealed several phases that reflected the composite material's structural and compositional gradient. The hexagonal hydroxyapatite $Ca_{10}(PO_4)_6(OH)_2$ phase was clearly identified, with its characteristic peaks appearing at angles 2θ ≈ 25.9°, 31.7°, 32.2°, and 32.9° corresponding to the crystalline planes (002), (211), (112), and (300), respectively. This confirms the preservation of the stable crystalline structure of HA after preparation and heat treatment. Additional peaks were also observed at 2θ ≈ 39.8°, 46.7°, and 49.5° corresponding to levels (310), (222), and (213), indicating

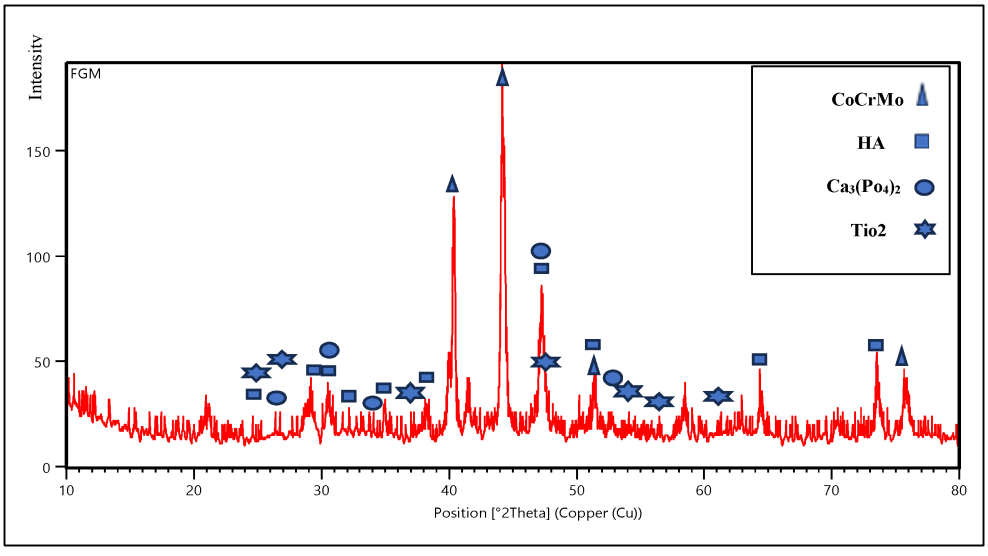

Fig. 4. The X-ray diffraction patterns of the sample FGM.

Table 3. The X-ray diffraction pattern of hydroxyapatite powder.

Dislocation distance $(nm)^{-2}$	strain(ε) × 10^{-3}	Grain size(D) (nm)	FWHM (deg)	Orientation	d (nm)	2-Theta (deg)
8.149	2.76	55.9	0.143	(002)	0.3503	25.436
8.158	3.13	49.3	0.162	(002)	0.3501	25.420
8.717	10.53	14.0	0.568	(102)	0.3387	26.494
10.372	7.02	19.5	0.412	(210)	0.3105	28.736
11.390	4.86	26.0	0.300	(210)	0.2963	30.135
12.593	4.37	27.8	0.285	(211)	0.2818	31.752
12.884	3.71	31.7	0.252	(300)	0.2786	32.999
14.403	2.96	30.4	0.262	(202)	0.2635	34.044
17.289	2.73	36.7	0.229	(310)	0.2405	37.273
26.488	2.65	31.0	0.270	(222)	0.1943	46.704

a good degree of crystallinity of the BioPhase [14]. In addition, the presence of the calcium phosphate β-TCP ($Ca_3(PO_4)_2$) phase was detected through its peaks located at 2θ ≈ 27.7°, 31.0°, 34.4°, and 47.1°, corresponding to levels (214), (0210), (300), and (226), indicating partial decomposition of hydroxyapatite during heat treatment and the transformation of part of it into β-TCP, a phase known for its stimulating role in bone fusion due to its higher bio solubility [14]. The patterns also showed distinct peaks of titanium dioxide Tio_2 in the anatase phase at 2θ ≈ 25.3°, 37.8° and 48.0° corresponding to levels (101), (004) and (200), with a possible limited contribution of the rutile phase at 2θ ≈ 27.4° and 36.1°, reflecting surface oxidation of titanium during heat treatment, which enhances the biocompatibility and surface activity of the material [19]. As for the metallic phase, the presence of the hexagonal titanium phase α-Ti was confirmed by its peaks at 2θ ≈ 35.1°, 38.4°, and 40.2° corresponding to levels (100), (002), and (101), in addition to the peaks of the face-centered cubic Co–Cr–Mo alloy FCC at 2θ ≈ 44.2°, 51.4°, and 75.8° belonging to levels (111), (200), and (220) [20]. When sintered at 1000 °C, HA is not merely an inert layer but also undergoes thermochemical reactions with titanium and the F75 alloy, leading to the formation of bioactive phosphate and oxide phases. This explains the appearance of the β-TCP and Tio_2 phases in the XRD pattern.

3.1.3. Scanning electron microscope

A continuous functional gradient between ceramic and metallic phases in the layers of the F75/HA composite was successfully observed using a Scanning Electron Microscopy (SEM). EDS testing confirmed that the five-layer sample exhibited a more continuous, homogeneous gradient from the hyaluronic acid-rich top layer to the mineral bottom layer. Each layer represented a smoother compositional transition with a gradual decrease in porosity and a marked improvement in interlayer bond strength, as shown in Figs. 5–9. This increasing percentage of ceramic improves bio layers compatibility, reduces stress accumulation, the adhesion strength increases. At the top,

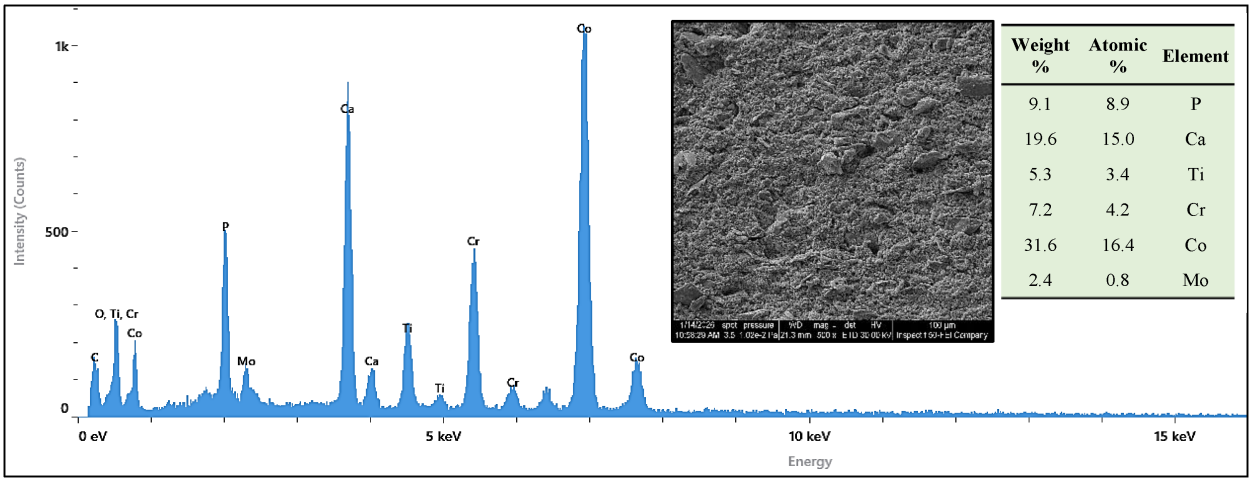

Weight %	Atomic %	Element
9.1	8.9	P
19.6	15.0	Ca
5.3	3.4	Ti
7.2	4.2	Cr
31.6	16.4	Co
2.4	0.8	Mo

Fig. 5. SEM Image and EDS analysis of the FGM - Layer 1 consists of 50 % F75 + 50 % HA.

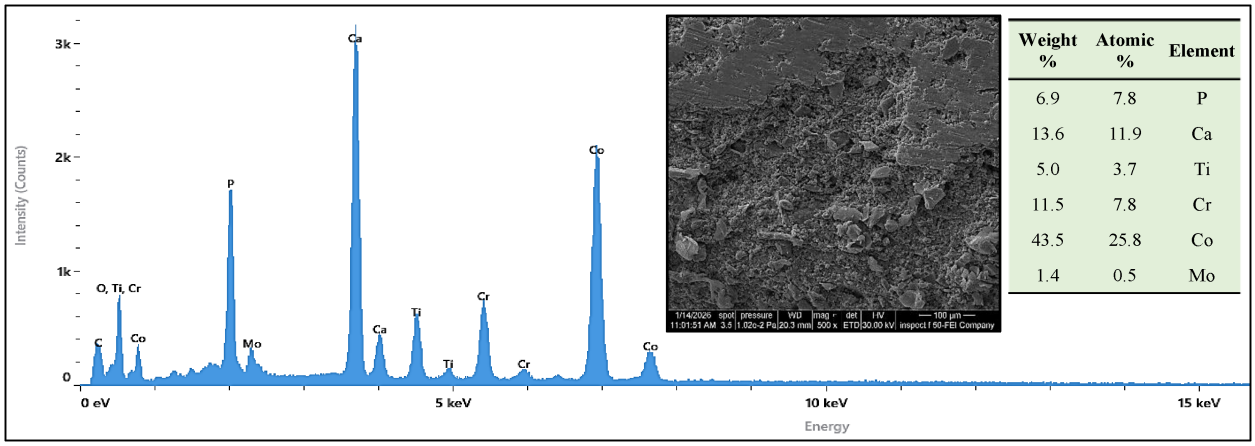

Weight %	Atomic %	Element
6.9	7.8	P
13.6	11.9	Ca
5.0	3.7	Ti
11.5	7.8	Cr
43.5	25.8	Co
1.4	0.5	Mo

Fig. 6. SEM Image and EDS analysis of the FGM - Layer 2 consists of 55 % F75 + 45 % HA.

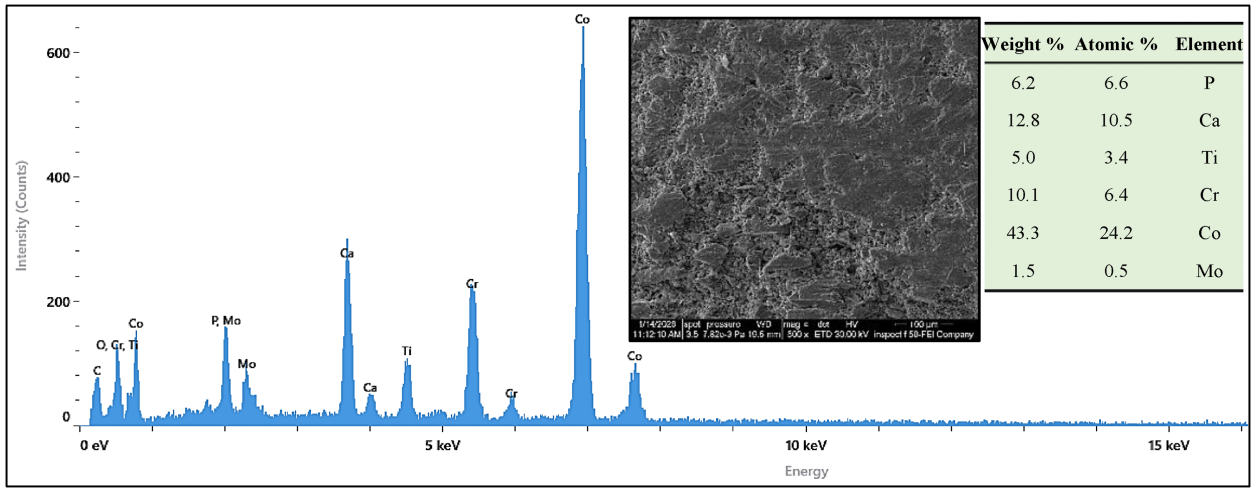

Weight %	Atomic %	Element
6.2	6.6	P
12.8	10.5	Ca
5.0	3.4	Ti
10.1	6.4	Cr
43.3	24.2	Co
1.5	0.5	Mo

Fig. 7. SEM Image and EDS analysis of the FGM - Layer 3 consists of 65 % F75 + 35 % HA.

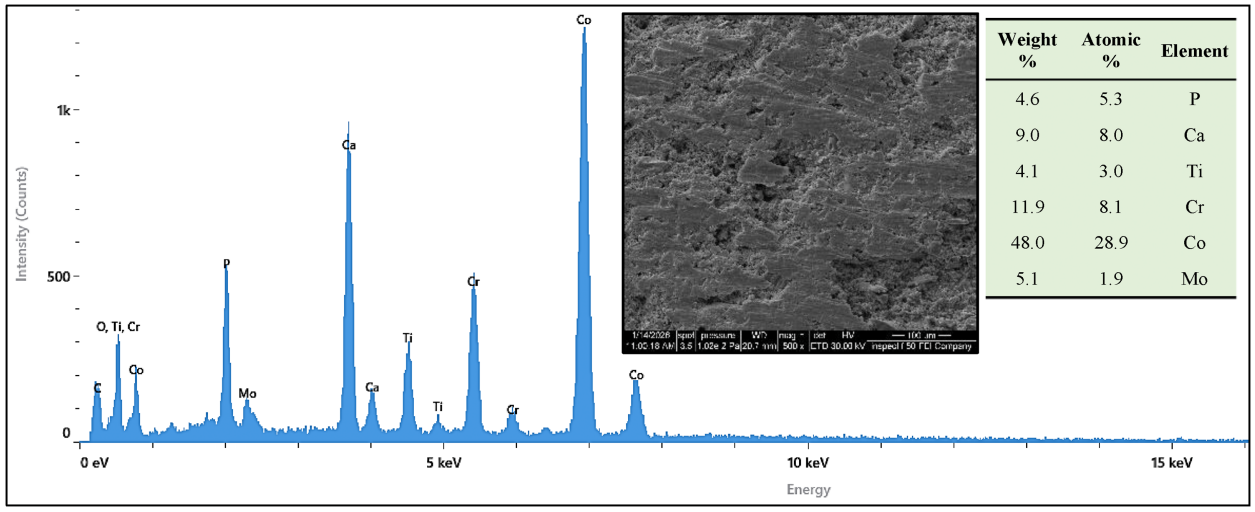

Weight %	Atomic %	Element
4.6	5.3	P
9.0	8.0	Ca
4.1	3.0	Ti
11.9	8.1	Cr
48.0	28.9	Co
5.1	1.9	Mo

Fig. 8. SEM Image and EDS analysis of the FGM-layer 4 consists of 75 % F75 + 25 % HA.

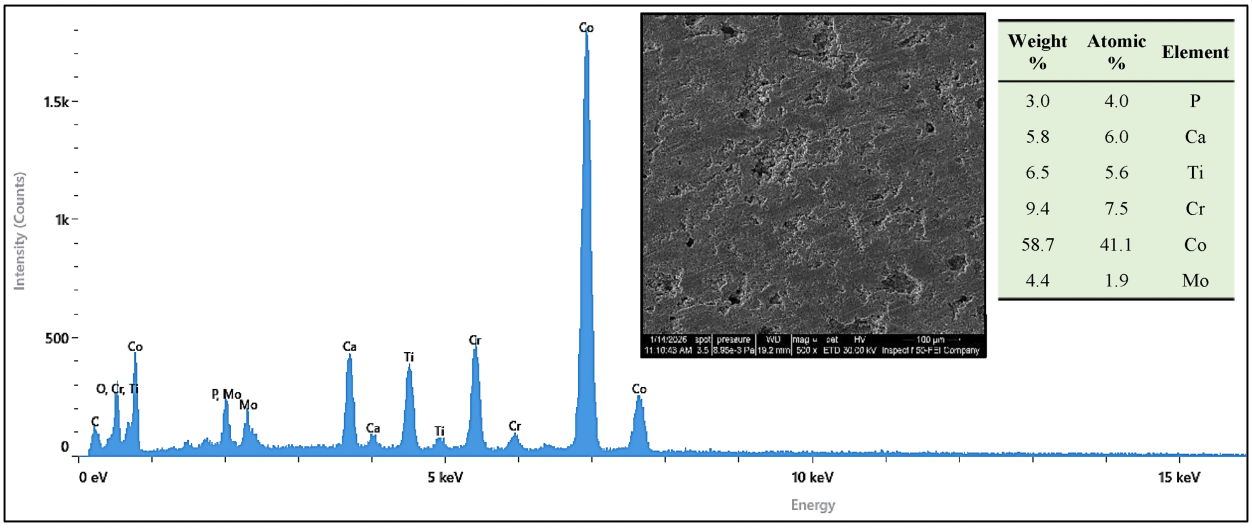

Weight %	Atomic %	Element
3.0	4.0	P
5.8	6.0	Ca
6.5	5.6	Ti
9.4	7.5	Cr
58.7	41.1	Co
4.4	1.9	Mo

Fig. 9. SEM Image and EDS analysis of the FGM-layer 5 consists of 85 % F75 + 15 % HA.

the pentagonal sample retains high bioactivity; the bottom layer is a metal layer, which is superior in mechanical hardness and durability, as reported by S. Daneshmand et al. [21].

In Fig. 5, a Scanning electron microscopy (SEM) image shows the analysis of the first layer of the functionally graded (FGM) sample, the CoCrMo region can be seen as a more cohesive and dense structure, whereas the HA region is seen as a granular, lumpy mass that looks like small rocks. The accompanying EDS spectrum confirms the presence of distinct peaks for calcium, phosphorus, and oxygen, thereby establishing the identity of the ceramic phase and indicating the successful integration of hydroxyapatite within the graded structure, with no evidence of interfacial separation or structural instability. The surface layer, rich in hydroxyapatite, exhibits a homogeneous structure with ceramic aggregates and higher porosity, which enhances biological properties and apatite deposition. As we move towards the intermediate layers (Figs. 6–9), the continuity of the mineral phase increases, clumps decrease, and porosity gradually decreases. The layers closer to the mineral core exhibit a denser structure and a clear dominance of the mineral phase, with only limited traces of hydroxyapatite remaining, providing greater mechanical support and better corrosion resistance. This EDS analysis confirms a gradient, with decreasing Ca and P peaks and increasing metallic peaks across the layers, demonstrating the success of the FGM design in achieving an effective balance between biological and mechanical requirements.

3.2. Mechanical properties

3.2.1. Microhardness

Fig. 10 illustrates the microhardness of FGM. The results showed a clear decrease in hardness values with increasing hydroxyapatite content within the mineral matrix. The fifth layer (15 % HA) recorded the highest hardness value of 375.63 ± 17.8 Hv, while the hardness decreased significantly with the addition of HA to 147.9 ± 6.7 Hv, and a continued

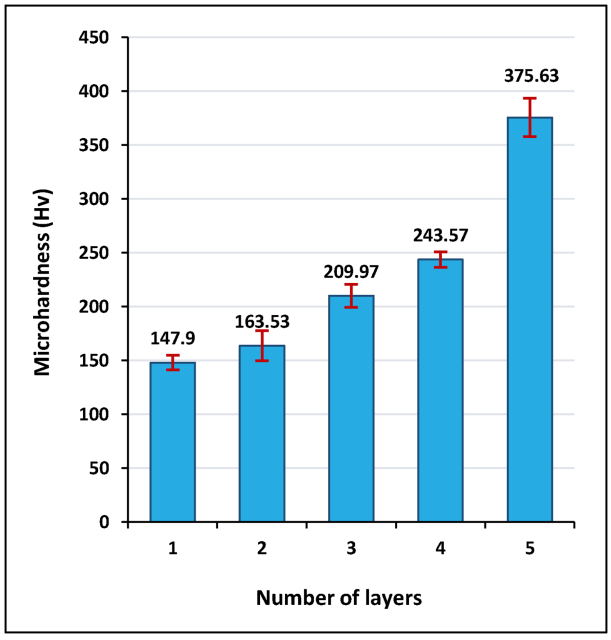

Fig. 10. The Microhardness of sample FGM with different layer compositions.

gradual decrease as the HA percentage increased. This behavior is attributed to the fact that increasing HA led to a higher apparent porosity and a lower bulk density of the composite, which reduces the material's resistance to penetration during the Vickers test [22]. Scanning electron microscopy (SEM) images also revealed a clear increase in pore size and number with increasing HA content, confirming that the porosity formed during the sintering process is a key factor in reducing hardness. Thus, the results indicate an inverse relationship between HA content and hardness values, suggesting that the addition of HA enhances the composite's biological properties.

The addition of titanium to the mineral composition leads to the inhibition of crystal slip movement, and this increases the resistance to plastic deformation. Also, in XRD examination, the formation of Tio_2 was very hard, chemically stable, corrosion-resistant. This greatly improves the hardness of the layers from which support is required. The FGM sample showed that graded functional engineering of materials is necessary to achieve the optimal balance between hardness and biological properties required for orthopedic applications.

3.2.2. Modulus of elasticity

This section presents the elastic characteristics of functionally graded specimens and contrasts them with those of the conventional F75 specimen. Elastic moduli are among the measured outcomes [23], which reflect each specimen's mechanical response under load.

The difference between the standard F75 alloy and the functionally graded sample FGM. Due to its dense and homogeneous metallic structure, the F75 alloy exhibited the highest values for Young's modulus, with a Young's modulus of approximately 220 ± 2.65 GPa. These values are consistent with ASTM F75 for Co–Cr–Mo alloys. Conversely, the mechanical values reduced considerably in the functionally graded sample. The Young modulus of sample FGM was about 34.37 ± 0.49 GPa. The calculated modulus of elasticity is close to that of cortical bone (20–30 GPa), indicating a reduction in stiffness mismatch and a limitation of stress blocking. Previous studies have shown similar results when Co–Cr–Mo or titanium alloys are reinforced with hydroxyapatite, where Bahrami et al. demonstrated that increasing the hydroxyapatite content leads to a decrease in the modulus of elasticity due to agglomeration and porosity [24]. Ultrasound technology is a non-destructive method for measuring the elastic properties of functionally graded materials, as it relies on the direct relationship among wave speed, material density, and elastic constants. This method is distinguished by measuring the volumetric elastic response of the entire sample rather than just the surface layers, as in nanoindentation, because waves propagate through the sample's entire thickness. The presence of multiple interfaces leads to partial scattering of wave energy and an increase in the effective transit time, which mathematically translates to a lower value for the modulus of elasticity. Furthermore, hydroxyapatite-rich layers are often associated with increased microporosity and granular agglomeration, which contributes to a reduction in the effective density observed by ultrasound.

3.3. Corrosion tests

Fig. 11 shows the potentiometric polarisation test of a functional graded material (FGM) sample in a simulated body fluid (SBF), in which the FGM sample exhibited stable electrochemical behavior and improved corrosion resistance. The corrosion current (Icorr) reached approximately 78.13 ± 0.85 μA, while the corrosion potential (Ecorr) was approximately −473 ± 2.65 mV, indicating decreased electrochemical activity and surface stability in the biological medium. Consequently, the corrosion rate (CR) was approximately 0.413 ± 0.015 mm/year, which is relatively low.

As shown in Fig. 11, the corrosion current decreases with increasing voltage until it reaches a minimum. The corrosion current increases with voltage during anodic polarisation until it reaches a constant value, at which point it drops sharply as a passive film forms. The passive film disintegrates as the voltage increases, thereby increasing the current again [25]. The abrupt increase in current at the pitting potential is sometimes due to localized activation within the protective film rather than to the instantaneous breakdown of the passive layer.

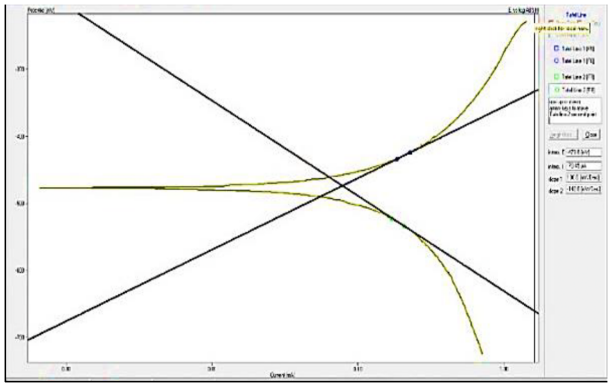

Fig. 11. Potentiodynamic polarization curves of FGM in SBF.

Before a stable pitting hole formed, this activation causes the current density to rise quickly. Since the development of microscopic active sites within the passive layer is necessary for the gradual transition from passive behavior to pitting, the current jump is more indicative of the onset of a localized disturbance than of the formation of a full-blown pit [25].

The biomedical material's resistance to corrosion and biocompatibility depend on numerous factors, such as electrolyte conditions, surface condition, chemical composition, and applied stress. One of the most important parameters in the material surface state is the surface electric property of the material, since these parameters determine the resistivity of materials [26]. The corrosion resistance of titanium is high because a stable titanium oxide (Tio_2) layer forms, acting as a passive barrier that prevents the metal from dissolving in the biocompatible environment. This results in a reduced corrosion current (Icorr) and a higher corrosion potential towards more favorable values. This synergy between Tio_2 and HA enhances the electrochemical stability of the implant and minimizes localized corrosion [26]. The five-layer sample (FGM) exhibits higher corrosion resistance due to the smooth gradient between the metal and ceramic layers, which reduces the electrochemical potential difference between them. Layers that reduce the electrochemical potential between them.

3.4. Biological and bioactivity tests

The FGM samples were prepared and placed in a liquid solution mimicking body fluid (SBF). The goal of this procedure is to assess the ability of samples to deposit a calcium phosphate coating, particularly a hydroxyapatite (HA) coating, which is a measure of biocompatibility and the capacity to interact with native bone. The surface was then analyzed with a scanning electron microscope (SEM-EDS) to define the morphological features of the surface and also analyze the structure of the surface after deposition of the HA layer, in addition to determining the distribution and homogeneity of the HA layer on the sample surface.

Fig. 12 presents scanning electron microscopy (SEM) images at various magnifications, revealing that the surface morphology of the FGM-labelled sample is well developed after 48 days in a solution representing body fluid (SBF). The surface appears

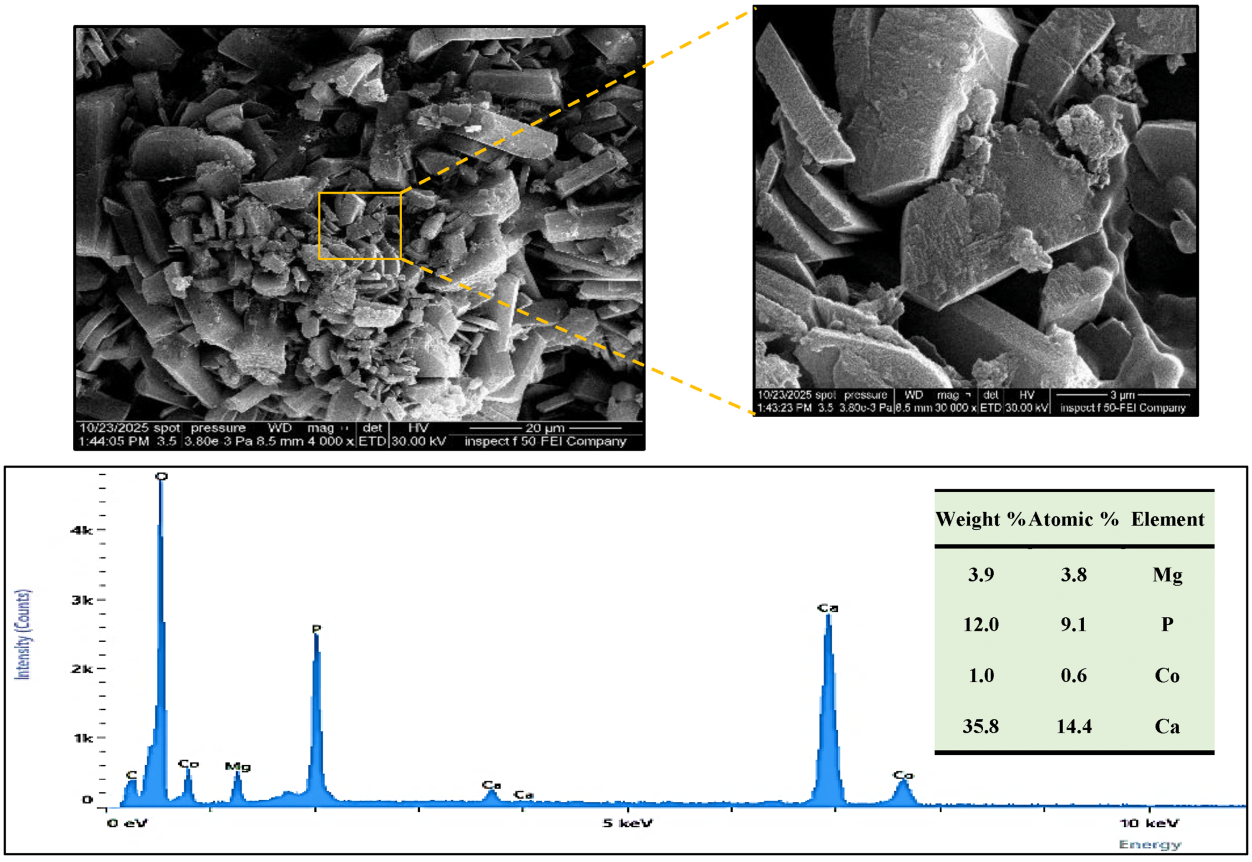

Fig. 12. Morphology of apatite formation induced on FGM at different magnifications.

to be almost entirely covered by a layer of calcium phosphate, ranging from fine aggregates with a primary morphology to large, cohesive, platy crystals, providing direct evidence of nucleation and the successive growth of bone-like hydroxyapatite. At high magnifications, the images show fine nanoclumps with needle-like and platy shapes, representing the early nucleation stage of apatite, where calcium and phosphate ions exchanged between the material surface and the solution begin to arrange themselves at the high-energy sites on the surface. As magnification decreases, the crystals become more distinct and regular, forming broad, interlocking sheets, indicating continuous growth of a crystalline, mature apatite layer covering the surface [11]. This morphological behavior is consistent with elemental spectroscopy (EDS), which showed elevated calcium and phosphorus concentrations at the surface, confirming the formation of a stable calcium phosphate layer. The calculated atomic ratio Ca/P ≈ is 1.54. It is close to the ratio of bone hydroxyl apatite (1.67), indicating the formation of a biological apatite phase, the most common form in normal bone. The analysis also revealed the presence of magnesium (Mg) in the surface layer. This element plays a vital role in modifying apatite morphology and increasing its bioavailability, thereby improving cell adhesion and promoting bone differentiation. The near-complete decrease in the cobalt (Co) signal indicates that the metallic surface of the inner layer is almost entirely covered by the formed apatite layer, which strongly indicates the efficiency of the FGM gradient surface in stimulating surface reactions and isolating essential metallic elements from the biological environment. Taken together, these results from morphological and chemical analyses confirm that the graded structure of sample FGM provides an efficient environment for nucleation and continuous growth of a stable bio-apatite layer, enhancing the material's ability to achieve long-term osteo-bonding and demonstrating its promise for implant applications.

The results of immersion in SBF solution showed that the addition of titanium to the graded structure based on Co–Cr–Mo and HA alloy significantly enhanced the surface's ability to catalyze hydroxyapatite formation over short time periods. When Ti is incorporated into the structure, a thin surface layer of Tio_2 (with anatase and rutile phases) is formed during sintering. This layer has high surface activity and can carry hydroxyl groups (-OH). These groups readily transform into positively charged sites upon contact with the physiological medium, creating a slightly positively charged surface that attracts and binds negatively charged phosphate ions (PO_4^{3-}), thereby accelerating apatite nucleation. This indicates the formation of a thicker, more crystalline HA layer on the surface. Furthermore, the appearance or increase in Ti–O peaks confirm the formation of a bioactive Tio_2 layer, which acts as an intermediate between the mineral surface and Ca–P deposition. Similarly, the X-ray diffraction (XRD) results supported these conclusions; the titanium-enhanced samples showed sharp, high-intensity diffraction peaks of the hydroxyapatite phase at (2θ) angles of approximately 29.2°, 30.1°, 33.0°, 34°, and 46.7° with a decrease in the half-maximum width (FWHM) of these peaks; this indicates a high degree of crystallinity and an increased thickness of the apatite layer formed. At the same time, distinct peaks of the Tio_2 phases (anatase near 25.3° and rutile near 27.4°) appeared, confirming the role of titanium in forming a stable oxide layer and effectively stimulating the subsequent growth of HA. Thus, titanium's contribution is not limited to modifying the mechanical properties of FGM but also clearly improves the biological response [20].

FGM and conventional F75 alloy were tested against Gram-negative bacteria, *Escherichia coli* (*E. coli*), and Gram-positive bacteria, *Staphylococcus aureus* (*S. aureus*), using antibacterial tests. Fig. 13 shows the performance of sample FGM and F75 in reference to the bacteria being tested. The results showed that the number of *Escherichia coli* colonies in the control group was $1.34 \pm 0.02 \times 10^8$ CFU/ml. The FGM sample decreased to $0.060 \pm 0.020 \times 10^8$ CFU/ml, while the F75 sample recorded $0.13 \pm 0.03 \times 10^8$ CFU/ml. Similarly, the *Staphylococcus aureus* control sample recorded $1.21 \pm 0.04 \times 10^8$ CFU/ml The numbers decreased to $0.100 \pm 0.026 \times 10^8$ CFU/ml for sample FGM, while the F75 sample recorded $0.13 \pm 0.03 \times 10^8$ CFU/ml. These findings demonstrate strong antibacterial activity of the samples, with FGM clearly superior at inhibiting the growth of Gram-negative and Gram-positive bacteria. These results confirm what S.S. Patel et al. concluded: cobalt-chromium alloys exhibit a higher biofilm-forming capacity than alloys containing titanium [27]. Studies indicate that chemically active, oxidized metal surfaces can induce the formation of reactive oxygen species (ROS) at the surface-solution interface. These reactive species disrupt bacterial cell membranes, oxidize proteins within them, and damage their genetic material, leading to impaired vital functions and cell death. A study by X. Hu et al. showed that titanium surfaces in the anatase phase possess antibacterial activity associated with ROS generation; in contrast, modified cobalt-chromium alloys (with the addition of titanium and HA) reduce bacterial adhesion primarily by altering the surface chemistry and

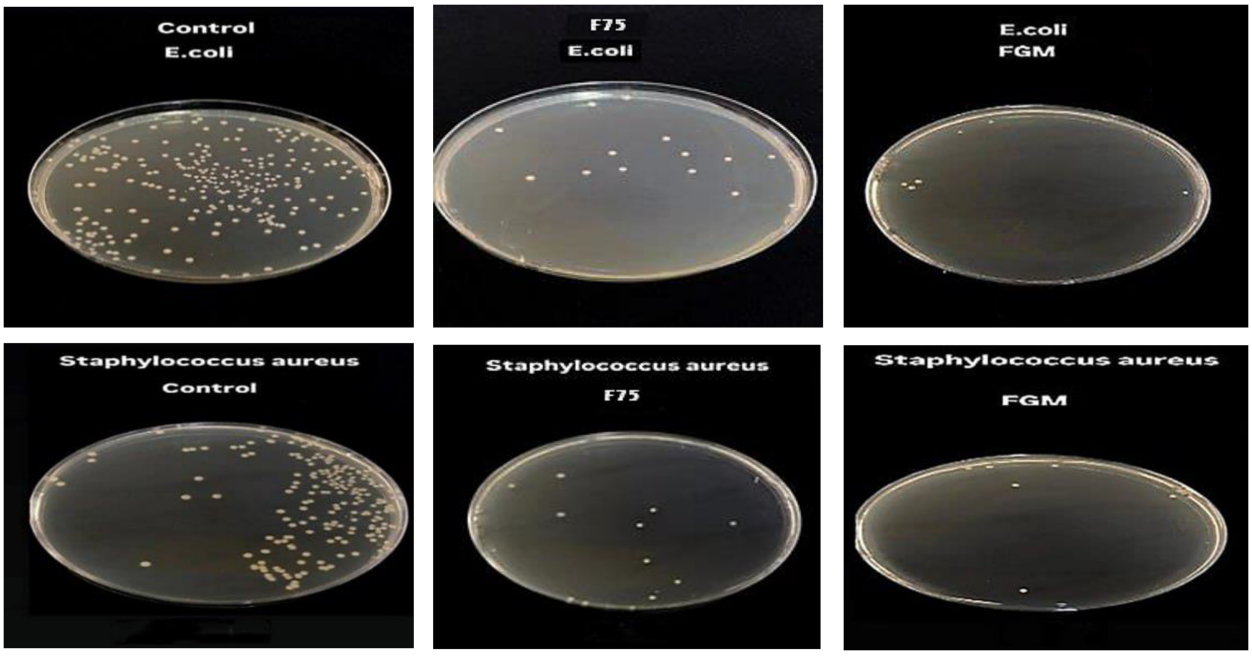

Fig. 13. Antibacterial activity of the F75 and FGM after 24 h.

increasing its hydrophilicity, without generating high levels of ROS or causing significant bone cell death, highlighting the importance of controlling ROS levels in applications such as bone implants [28].

4. Conclusions

Hydroxyapatite and titanium were added to a Co–Cr–Mo alloy to create a functionalized graded material with enhanced mechanical and biological characteristics, microstructure, and interfacial bonding. Sample FGM exhibited the highest hardness (375.63 ± 17.8 HV), enhanced wear resistance, and a Young's modulus comparable to that of cortical bone (34.37 ± 0.49 GPa), resulting in less stress shielding. Additionally, it demonstrated enhanced biological and antimicrobial activities, qualifying it for use in bone implant applications.

Ethics Information

Approval N0.BCSMU/1124/0006Ph, dated November 1,2024.

Funding

Funded by the authors.

Conflicts of interest

The authors declare that there are no financial, scientific, or personal conflicts of interest related to this research.

Acknowledgements

The authors express their thanks and gratitude to Mustansiriyah University for supporting the scientific laboratories by providing the necessary equipment for conducting experiments.

References

[1] L. Ladani, M. Palmieri, Review of the use of metals in biomedical applications: biocompatibility, additive manufacturing technologies, and standards and regulations, J. Metals 14 (9) (2024) 1039, https://doi.org/10.3390/met14091039.
[2] L. García, P. Alvaredo, J.M. Torralba, M. Campos, Material extrusion: a promising tool for processing CoCrMo alloy with excellent wear resistance for biomedical applications, J. Mater. Des. 244 (2024) 113089, https://doi.org/10.1016/j.matdes.2024.113089.
[3] R.F. Heary, N. Parvathreddy, S. Sampath, N. Agarwal, Elastic modulus in the selection of interbody implants, J. Spine Surg. 3 (2) (2017) 163, https://doi.org/10.21037/jss.2017.05.01.
[4] Y.C. Huang, P.C. Hsiao, H.J. Chai, Hydroxyapatite extracted from fish scale: effects on MG63 osteoblast-like cells, J. Ceramic. Int. 37 (6) (2011) 1825–1831, https://doi.org/10.1016/j.ceramint.2011.01.018.
[5] I. Redhwi, A. Fallatah, F. Alshabona, Hydroxyapatite: a comprehensive review of its properties, applications, and future trends, Int. J. Biomed. Mater. Res. 12 (1) (2024) 1–6, https://doi.org/10.11648/j.ijbmr.20241201.11.
[6] H. Rack, J. Qazi, Titanium alloys for biomedical applications, Mater. Sci. Eng. C 26 (8) (2006) 1269–1277, https://doi.org/10.1016/j.mse.c.2005.08.032.
[7] H. Shi, P. Zhou, J. Li, C. Liu, L. Wang, Functional gradient metallic biomaterials: techniques, current scenery, and future prospects in the biomedical field, J. Front. Bioeng. Biotechnol. 18 (2021) 616845, https://doi.org/10.3389/fbioe.2020.616845, 2020.

[8] Z. Doni, A. Alves, F. Toptan, L. Rocha, M. Buciumeanu, L. Palaghian, F.S. Silva, Tribocorrosion behaviour of hot pressed CoCrMo− HAP biocomposites, J. Tribol. Int. 91 (2015) 221–227, https://doi.org/10.1016/j.triboint.2015.04.009.
[9] M. Fellah, N. Hezil, D. Bouras, A. Obrosov, A.S. Mohammed, A. Montagne, S. Wieb, Structural, mechanical and tribological performance of a nanostructured biomaterial Co–Cr–Mo alloy synthesized via mechanical alloying, J. Mater. Res. Technol. 25 (2023) 2152–2165, https://doi.org/10.1016/j.jmrt.2023.06.031.
[10] B. Bolborea, C. Baera, S. Dan, A. Gruin, D.D. Bur duhos-Nergis, V. Vasile, Concrete compressive strength by means of ultrasonic pulse velocity and moduli of elasticity, Materials 14 (22) (2021) 7018, https://doi.org/10.3390/ma14227018.
[11] F. Baino, S. Yamaguchi, The use of simulated body fluid (SBF) for assessing materials bioactivity in the context of tissue engineering, review and challenges, J.Biom. 5 (4) (2020) 57, https://doi.org/10.3390/biomimetics5040057.
[12] S. Jeanson, J. Floury, V. Gagnaire, S. Lortal, A. Thierry, Bacterial colonies in solid media and foods: a review on their growth and interactions with the micro-environment, J. Front. Microbiol. 6 (2015) 1284, https://doi.org/10.3389/fmicb.2015.01284.
[13] C. Yoganand, V. Selvarajan, J. Wu, D. Xue, Processing of bovine hydroxyapatite (HA) powders and synthesis of calcium phosphate silicate glass ceramics using DC thermal plasma torch, J .Vacuum 83 (2) (2008) 319–325, https://doi.org/10.1016/j.vacuum.2008.06.003.
[14] M. Manoj, R. Subbiah, D. Mangalaraj, N. Ponpandian, C. Viswanathan, K. Park, Influence of growth parameters on the formation of hydroxyapatite (HAp) nanostructures and their cell viabilitystudies, J.Nanbomedcine. 2 (11) (2015) 333–349, https://doi.org/10.5772/60116.
[15] P.O. Etinosa, O.A. Osuchukwu, E.O. Anisiji, M.Y. Lawal, S. A. Mohammed, O.I. Ibitoye, P.G. Oni, V.D. Aderibigbe, T. Aina, D. Oyebode, S.C. Nwigbo, In-depth review of synthesis of hydroxyapatite biomaterials from natural resources and chemical regents for biomedical applications, Arab. J. Chem. 17 (12) (2024) 106010, https://doi.org/10.1016/j.arabjc.2024.106010.
[16] I. Ielo, G. Calabrese, G. De Luca, S. Conoci, Recent advances in hydroxyapatite-based biocomposites for bone tissue regeneration in orthopedics, Int. J. Mol. Sci. 23 (17) (2022) 9721, https://doi.org/10.3390/ijms23179721.
[17] S. Rattan, D. Fawcett, G.E.J. Poinern, Williamson–Hall based X-ray peak profile evaluation and nano-structural characterization of rod-shaped hydroxyapatite powder for potential dental restorative procedures, J. AIMS Mater. Sci.. 8 (3) (2021) 359–372, https://doi.org/10.3934/matersci.2021023.
[18] K. Venkatachalam, M. Sandhyarani, T. Nellaippan, N. Rameshbabu, Estimation of crystallite size, lattice strain and dislocation density of nanocrystalline carbonate substituted hydroxyapatite by X-ray peak variance analysis, J. Procedia. Mater. Sci. 5 (2014) 212–221, https://doi.org/10.1016/j.mspro.2014.07.260.
[19] S. Yamaguchi, H. Hashimoto, R. Nakai, H. Takadama, Impact of surface potential on apatite formation in Ti alloys subjected to acid and heat treatments, J. Mater. 10 (10) (2017) 1127, https://doi.org/10.3390/ma10101127.
[20] K. Yoda, A. Takaichi, N. Nomura, Y. Tsutsumi, H. Doi, S. Kurosu, A. Chibo, Y. Igarashi, T. Hanawa, Effects of chromium and nitrogen content on the microstructures and mechanical properties of as-cast Co–Cr–Mo alloys for dental applications, J. Acta Biomaterialia. 8 (7) (2012) 2856–2862, https://doi.org/10.1016/j.actbio.2012.03.024.
[21] S. Daneshmand, M.H. Vini, A. Basem, N.S.S. Singh, M.A. Hussein, S. Salahshour, A. Mokhtari, Production of Ti/HA functionally graded material implants using powder metallurgy technique for reduction of the effect of chemical pollution, J. Ain ShamsEngineering 16 (10) (2025) 103573, https://doi.org/10.1016/j.asej.2025.103573.
[22] S. W Lee, Y. Kim, H.T. Rho, S-i. Kim, Microhardness and microstructural properties of a mixture of hydroxyapatite and β-tricalcium phosphate, J. Asian Ceramic Soc. 11 (1) (2023) 11–17, https://doi.org/10.1080/21870764.2022.2136261.
[23] A.M. da Rocha, T.C. Dourado, S.A. Miquelet, R.L. Gaiofatto, R.F. Costa-Felix, Evaluation of the elastic modulus of concrete using non-destructive ultrasonic methods and the natural vibration method, J. Acta IMEKO. 14 (3) (2025) 1–6, https://doi.org/10.21014/actaimeko.v14i3.2024.
[24] M. Bahrami, M. Fathi, M. Ahmadian, The effect of nano-bioceramic reinforcement on mechanical and biological properties of Co-base alloy/hydroxyapatite nanocomposite, J. Mater. Sci. Eng. C. 48 (2015) 572–578, https://doi.org/10.1016/j.msec.2014.12.017.
[25] J.R. Scully, N.D. Budiansky, Y. Tiwary, A.S. Mikhailov, J.L. Hudson, An alternate explanation for the abrupt current increase at the pitting potential, J. Cor. Rosion Sci. 50 (2) (2008) 316–324, https://doi.org/10.1016/j.corsci.2007.08.002.
[26] A. Jaafar, C. Hecker, P. Árki, Y. Joseph, Sol-gel derived hydroxyapatite coatings for titanium implants: a review, J. Bioeng. 7 (4) (2020) 127, https://doi.org/10.3390/bioengineering7040127.
[27] S.S. Patel, W. Aruni, S. Inceoglu, Y.T. Akpolat, G.D. Botimer, W.K. Cheng, O.A. Danisa, A comparison of Staphylococcus aureus biofilm formation on cobalt-chrome and titanium-alloy spinal implants, J. Clin. Neurosci. 31 (2016) 219–223, https://doi.org/10.1016/j.jocn.2016.03.013.
[28] X. Hu, K.G. Neoh, J. Zhang, E.T. Kang, Bacterial and osteoblast behavior on titanium, cobalt–chromium alloy and stainless steel treated with alkali and heat: a comparative study for potential orthopedic applications, J. Colloid Inter. Sci. 417 (2014) 410–419, https://doi.org/10.1016/j.jcis.2013.11.062.